Surfactant–Free, Stable Noble Metal–Graphene Nanocomposite as High Performance Electrocatalyst

2 AUTHORS:

Avijit Mondal
Indian Association for the Cultivation of Scie…
8 PUBLICATIONS **89** CITATIONS

SEE PROFILE

Nikhil R Jana
Indian Association for the Cultivation of Scie…
113 PUBLICATIONS **10,066** CITATIONS

SEE PROFILE

# Surfactant-Free, Stable Noble Metal−Graphene Nanocomposite as High Performance Electrocatalyst

Avijit Mondal and Nikhil R. Jana*

Centre for Advanced Materials, Indian Association for the Cultivation of Science, Kolkata-700032, India

S *Supporting Information*

ABSTRACT: Preparation of a noble metal−graphene nanocomposite (MGN)-based clean and stable catalyst with uniform distribution of ultrafine nanoparticles can greatly improve the performance of fuel cells. Here, we show that surfactant-free MGNs for different noble metals can be prepared for high-performance fuel cell catalysis by the reaction of respective ultrasmall colloidal metal oxide/hydroxides with partially reduced colloidal graphene oxide. The resultant MGN is composed of highly dispersed M−M^{+n} based nanoparticles of ultrasmall size and produces a strong and stable catalytic current for ethanol and formic acid oxidation.

KEYWORDS: *graphene, nanoparticle, nanocomposite, catalyst, fuel cell*
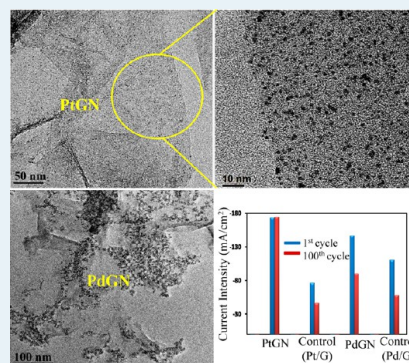
■ INTRODUCTION

Development of a high performance fuel cell catalyst has attracted extensive attention to exploring alternative green energy sources.[1] Noble metal based nanoparticles are used as a most efficient fuel cell catalyst, and it is now well established that a small particle size with a high surface area and accessible metal surface can greatly improve catalytic performance.[2] However, nanoparticles have a high surface energy with an inherent tendency to minimize their energy via aggregation.[3] Thus, nanoparticles are generally capped with various stabilizers[4] (e.g., surfactant,[4a] polymer,[4c] dendrimers,[4d] ligands[4b]), and these stabilizers severely limit the catalytic performance by lowering the accessibility of surface metal atoms.[5] To overcome this issue, noble metal nanoparticles are dispersed on various solid supports that can stabilize nanoparticles as well as increase the accessibility of nanoparticle surface.[6]

Recently, graphene has been explored as a promising 2D catalyst support due to its enormous surface area (2000−3000 m^{2}g^{-1}), high conductivity (10^5 to 10^6 Sm^{-1}), good mechanical strength, and good thermal stability.[7] Metal and semiconductor nanoparticle based composites with graphene have been synthesized and shown to improve electrocatalysis, photocatalysis, catalytic organic transformation, and efficient solar energy conversion.[7] Similarly, graphene based composites with Pt, Pd, and Au have been explored as fuel cell electrocatalysts[8] for efficient methanol oxidation,[8a,d,f] formic acid oxidation,[8b,c] and oxygen reduction reaction.[6c,8e,f,h] These results show that graphene can be a better fuel cell catalyst support than conventionally used carbon black. However, the poor solubility of graphene and weak interaction with nanoparticles contribute a major challenge in preparing homogeneous loading of nanoparticles and in stabilizing the nanocomposite.[8b,9] In common approaches, chemically synthesized colloidal graphene oxide is physically or chemically linked with nanoparticles via hydrophobic interaction, electrostatic interaction, or covalent bonding. Although these approaches offer homogeneous loading and attachment of nanoparticles on a graphene surface, an additional linker molecule/surfactant/polymer is essential to stabilize the nanocomposite.[2a,b,8b,d] For example, currently available Pt-graphene based composites are composed of surfactant stabilizers, and these stabilizer molecules partially block the catalytic sites, lower the catalytic efficiency, and are unable to stabilize the nanocomposite for repeated catalytic cycles.[8c,d] Moreover, Pt nanoparticles are prepared separately prior to producing graphene based composites, and thus the size of the Pt nanoparticles is limited by the colloid-chemical roots and is larger than 2.5 nm, along with a broad size distribution.[2b,6b,8a] Although there is a recent report on atomic layer deposition based synthesis of Pt−graphene composites having single atom and subnanometer Pt clusters, the catalytic current for methanol oxidation is shown to decrease after repeated cycles.[8f] Thus, it would be ideal to prepare graphene based composites with Pt, Pd, and Au with uniformly distributed ultrafine nanoparticles that are free from capping/stabilizing molecules and produce a strong and stable catalytic current under repeated cycles.

Here, we show that a surfactant-free Pt/Pd/Au/Ag-graphene nanocomposite can be prepared for high-performance fuel cell catalysis by a simple one step reaction of respective colloidal metal oxide/hydroxides with partially reduced colloidal graphene oxide. Resultant PtGN/PdGN produces a strong and stable catalytic current for ethanol and formic acid oxidation beyond 100 cycles. Our results show that the colloidal form of ultrafine metal oxide/hydroxide offers increased adsorption on partially reduced graphene oxide surfaces, and the reduced form of graphene oxide offers partial reduction of metal oxide/hydroxides in the absence of any external reducing agent. Such an *in situ* reduction of platinum oxide produces a graphene based stable nanocomposite with highly dispersed Pt−Pt^{II}−Pt^{IV} based nanoparticle 2.2 nm in size. Similarly, PdGN is composed of 3.4 nm size Pd based nanoparticles, AgGN is composed of 9 nm Ag based nanoparticles, and AuGN is composed of 26 nm Au based nanoparticles. Developed PtGN and PdGN have all three advantages required for fuel cell catalysts: First, the catalyst produces a strong and stable current for repeated cycles. Second, the catalyst can be used for ethanol and formic acid oxidation with significant tolerance of carbon monoxide poisoning effects. Third, the synthetic method is simple, and the catalyst can be preserved in solid form without any significant loss of activity. The comprehensive study of reported literature on graphene or graphene oxide based noble metal nanocomposites clearly shows the advantages of our method (Table S1).

■ EXPERIMENTAL SECTION

Materials and Reagents. Graphite powder (<20 μm), hydrazine monohydrate (98%), hexachloroplatinic acid hexahydrate (H$_2$PtCl$_6$·6H$_2$O), gold(III) chloride, palladium(II) chloride, and Pt on graphitized carbon (Pt/C, 20 wt %) were purchased from Sigma Aldrich and used as received. Silver nitrate, formic acid, sulphuric acid (98%), and activated carbon were purchased from Merck, India. All other reagents were of analytical grade and used without further purification. All the solutions were prepared by using double-distilled water.

Materials Synthesis. Graphene oxide was prepared by a modified Hummer's method,[7e] and stock solution was made with a concentration of ∼1.5 mg/mL. About 20 μL of hydrazine was added to 1.2 mL of graphene oxide solution and heated at 80−90 °C with constant stirring for 45 min. Resultant partially reduced graphene oxide was purified by adding 100 μL of NaCl solution (150 mg/mL) followed by centrifugation and repeated washing of the precipitate with pure water to remove any free reagents. The precipitate was redispersed in 1.2 mL of distilled water by ultrasonication.

Different sets of 1.5 mL solution of H$_2$PtCl$_6$ (10 mM) were prepared, and in each of the solutions, a different amount (0−75 μL) of NaOH solution (1 M) was added. Next, each solution was vortexed for 10−15 min and kept undisturbed at room temperature for 28 h. Colloidal platinum oxides are formed at this stage. Next, 400 μL of colloidal platinum oxides was mixed with 1.2 mL of partially reduced graphene oxide solution with 1−2 min ultrasonication followed by stirring for 6 h. Resultant PtGN dispersion was used as a stock solution for further experiments.

Similarly, a 1.0 mL solution of 10 mM palladium chloride or gold chloride or silver nitrate was thoroughly mixed with 2−150 μL of NaOH (1 M), and stirring was continued for 210, 40, and 10 min, respectively, to prepare the respective metal oxide colloids. A light yellow color appears for palladium and silver solutions, but the gold solution was colorless. Next, 400 μL of colloidal metal oxide/hydroxide solution was mixed with 1.2 mL of colloidal solution of partially reduced graphene oxide. The mixture was ultrasonicated for 1−2 min followed by 6 h of stirring. The resultant PdGN/AuGN/AgGN was purified by centrifugation and used for different experiments.

In control experiments (Table S2), 400 μL of H$_2$PtCl$_6$ (10 mM) or 400 μL of palladium chloride (10 mM) was mixed with 1.2 mL of partially reduced graphene oxide solution or activated carbon dispersion (1.5 mg/mL) followed by the addition of 200 μL of sodium borohydride solution (5 mg/mL) and stirred for 1 h. The resultant control 1/3/4 was centrifuged and washed several times with pure water. In another control experiment, 400 μL of gold chloride solution mixed with 1.2 mL of partially reduced graphene oxide followed by 1 h of stirring, and the resultant control 5 solution was purified by repeated centrifugation−washing. The final products were dispersed in 400 μL of water with ultrasonication.

Materials Characterization. Absorbance of the sample solutions was measured using an Agilent 8453 UV−visible spectrometer. X-ray diffraction (XRD) patterns were obtained using a Bruker D8 advance powder diffractometer using Cu Kα (λ = 1.54 A°) as the incident radiation. A microscopic image of the sample was observed with the JEOL-JSM-6700 Field Emission Scanning Electrone Microscope (FE-SEM). Transmission electron microscopic (TEM) samples were prepared by putting a drop of particle dispersion on a carbon coated copper grid and observed with an FEI Tecnai G2 F20 microscope. Raman spectra were recorded using an Agiltron R3000 Raman spectrometer with a 785 nm excitation laser and JY Horiba T64000 Raman spectrometer with a 514.5 nm excitation laser. X-ray photoelectron spectroscopy was performed using an Omicron (Serial No. 0571) X-ray photoelectron spectrometer. The amount of metal present in the composite materials was measured by Optima 2100 DV (Perkin-Elmer) inductively coupled plasma atomic emission spectroscopy (ICP-AES).

Electrochemical Measurements. A GCE of 3 mm in diameter (surface area of 0.07 cm^2) was carefully polished with 1, 0.3, and 0.05 μm alumina powder, sequentially, until a mirror finish was obtained. Next, the electrode was ultrasonically cleaned with ethanol and deionized water and dried in the air at room temperature. Then, the electrode was immersed in 0.5 M H$_2$SO$_4$ and was voltammetrically scanned from −0.4 to 1.2 V (vs Ag/AgCl) at a rate of 100 mV s$^{−1}$ to clean the surface. Finally, the composite dispersion was dropped onto the GCE surface, dried in the air at room temperature for 2 h, and used for electrochemical measurements. In the case of the control 2 sample, 0.5 wt % of nafion solution was used for electrode modification for better binding with the electrode surface. The loadings of Pt in PtGN, control 1, control 2, and control 3 on GCE were 4.37 μg, 4.87 μg, 5.95 μg, and 5.09 μg, respectively. Electrochemical measurements were performed with a CHI633D Electrochemical Analyzer. A conventional three-electrode system was used for all electrochemical experiments, which consisted of a platinum wire as an auxiliary electrode, an Ag/AgCl/saturated KCl as a reference electrode, and modified glassy carbon as a working electrode. All experiments were conducted at room temperature. For the electro-oxidation of formic acid, the cyclic voltamograms were recorded at a sweep rate of 50 mV/s in a mixture of H$_2$SO$_4$ (0.5 M) and formic acid (0.25 M). For the electro-oxidation of ethanol, the cyclic voltamm-grams were recorded at a sweep rate of 50 mV/s in a mixture of ethanol (0. 5M) and KOH (1 M). All the potentials were reported with respect to reversible hydrogen electrode (RHE).

■ RESULTS

Synthesis and Characterization of Noble Metal−Graphene Nanocomposite. The synthetic procedure is shown in Scheme 1, and details of characterization are shown in Figures 1 and 2 and the Supporting Information (Figures S1−S14). Colloidal metal oxide/hydroxide and partially reduced colloidal graphene oxide have been synthesized separately, and then their colloidal dispersions were mixed together in making MGN. Resultant MGN is then isolated as solid by simple centrifuge or decantation. The solid MGN can be redispersed in fresh water via sonication and deposited on an

Scheme 1. Schematic Representation of Synthesis Approach for Noble Metal−Graphene Nanocomposite
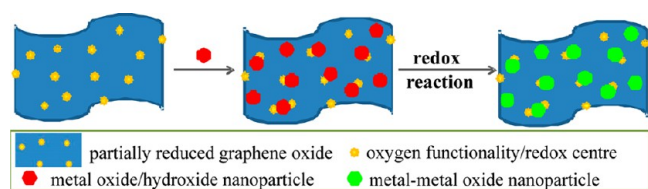
electrode surface whenever necessary. Colloidal platinum oxide[10a,c] (commonly known as Adam's catalyst) of ultrafine size has been synthesized by adjusting the pH of aqueous solution of H_2PtCl_6 in the absence of any surfactants. The

synthetic condition of colloidal platinum oxide has been optimized by varying the solution pH and reaction time. We found that a solution pH of 5.0 and overnight standing produces the best colloids in terms of small size and good colloidal stability. Solution color changes from yellow to brownish yellow upon adjusting the pH to 5 by adding NaOH. The UV−visible spectra show the appearance of a broad band at 250−350 nm range with a gradual decrease of the 260 nm peak, indicating the formation of platinum oxide/hydroxide[10a,b] (Supporting Information, Figure S1). Colloidal platinum oxide has been characterized by XRD and TEM. However, dialyzed colloids are unstable and precipitate from solution, suggesting that salts are responsible for colloidal stability. TEM study shows that particles are quite uniform with an average size of
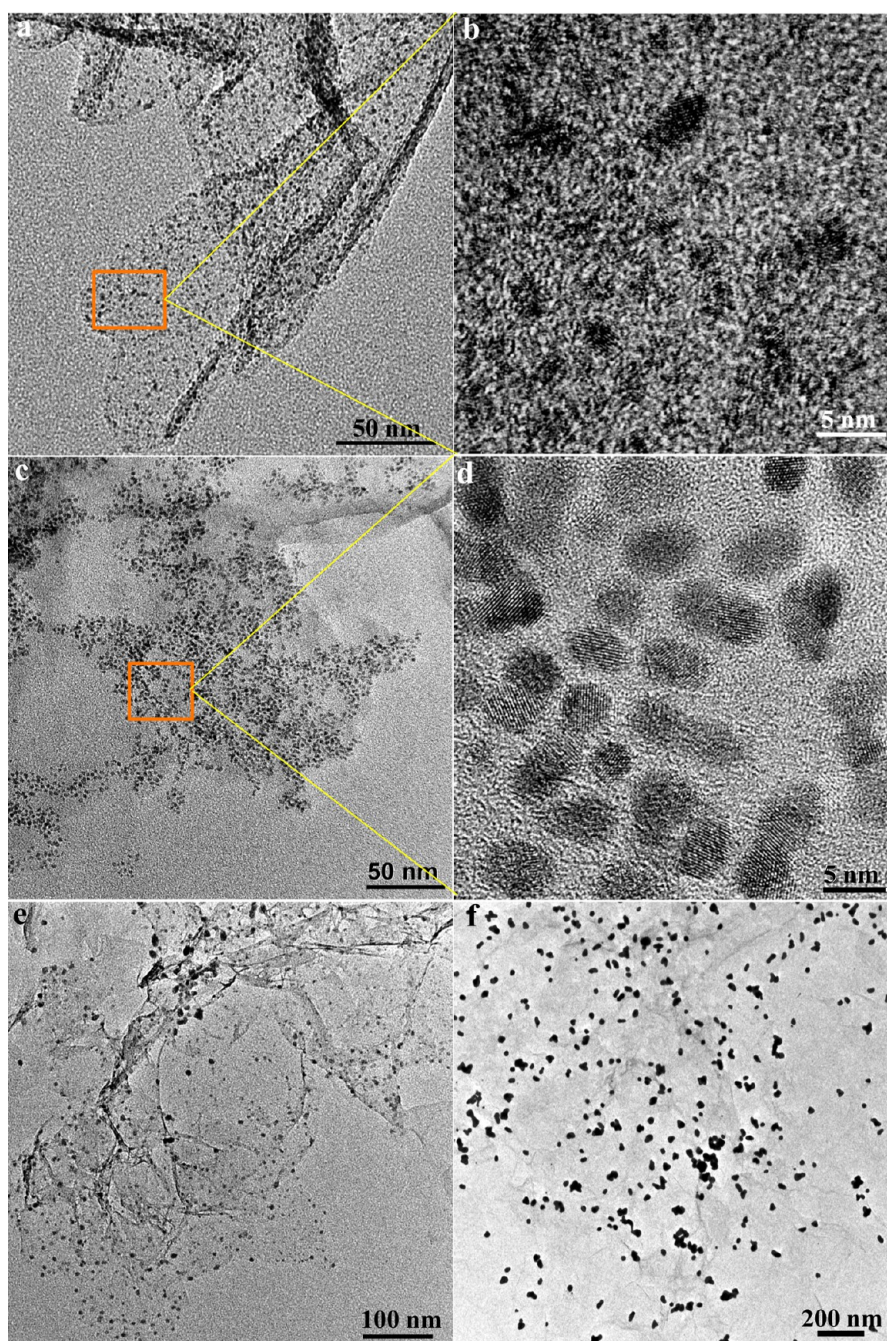

Figure 1. TEM image of graphene based composite with Pt (a,b), Pd (c,d), Ag (e), and Au(f).
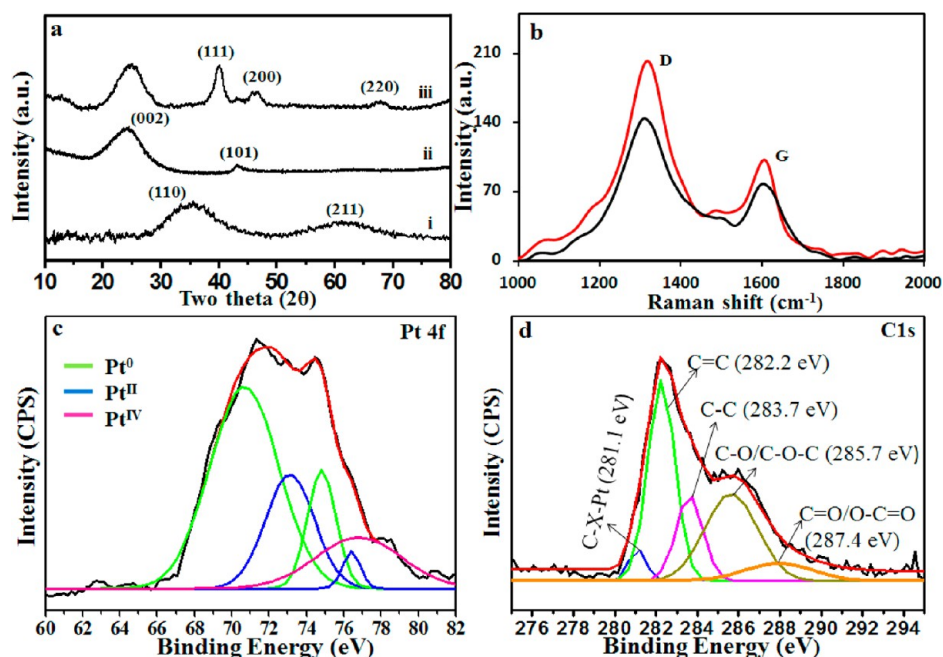
Figure 2. (a) XRD spectra of colloidal Pt^{IV} oxide (i), partially reduced graphene oxide (ii), and PtGN (iii). (b) Raman spectra of PtGN (red line) in comparison to partially reduced graphene oxide (black line). (c) XPS spectra of Pt 4f in PtGN showing that platinum nanoparticles consist of Pt^0, Pt^{II}, and Pt^{IV}. Deconvoluted Pt 4f spectrum displays five fitted signals at 70.7 eV (Pt $4f_{7/2}$) and 74.7 eV (Pt $4f_{5/2}$) corresponding to Pt^0, 73.1 eV (Pt $4f_{7/2}$) and 76.3 eV (Pt $4f_{5/2}$) corresponding to Pt^{II}, and 77.0 eV attributed to Pt^{IV}, and (d) XPS spectra of C 1s of PtGN showing different signatures of carbon atoms in deconvoluted nature.

2.3 nm. Colloidal oxide/hydroxide of Pd^{II}, Au^{III}, and Ag^{I} has been synthesized using the same strategy with some modifications by changing the amount of base or solution pH (Supporting Information).

The hybrid nature and property of individual components of PtGN have been characterized by XRD, TEM, Raman, and XPS. The TEM of PtGN shows that Pt nanoparticles are uniformly distributed on the surface of graphene, and Pt nanoparticles are highly monodispersed with an average size of 2.2 nm (Figure 1). The high resolution TEM image shows that each crystalline Pt nanoparticle is surrounded by a low contrast amorphous interface and is firmly grafted with graphene. Similar hybrid structures are also observed for PdGN with a uniform distribution of Pd based crystalline particles of 3.4 nm (Figure 1). The uniform distribution of metal particles was also observed in AgGN and AuGN, although the particle sizes are relatively large. The XRD of the dialyzed sample shows two broad reflection peaks corresponding to platinum(IV) oxide (Figure 2). The XRD of partially reduced graphene oxide shows the reflections of graphite planes; the MGN shows reflections for both graphite and the respective metal. The Raman spectra of MGN show a G band at 1600 cm^{-1} corresponding to the sp^2 hybridized carbon atoms and the D band at 1310 cm^{-1} corresponding to disruption of the sp^2 hybridized carbon atoms. The intensity ratio of the D band to the G band (I_D/I_G) for different MGNs lies between 1.98 and 2.13, which are little larger than the 1.84 of partially reduced graphene oxide or larger than the 1.14 of graphene oxide, and is attributed to the increased defects in graphene structure via electronic interaction with metal nanoparticles[10d,e] (Figure 2 and Supporting Information Figure S12). The interaction occurs between different functional groups of partially reduced graphene oxide and the oxide layer of metal. In addition, there

may be interaction between the π orbital of graphene with the vacant orbital of the noble metal.[10f]

X-ray photoelectron spectra (XPS) of PtGN and PdGN have been performed to determine the chemical environment and oxidation state of Pt and carbon (Figure 2 and Supporting Information Figures S13 and S14). Deconvoluted Pt 4f spectra of PtGN show peaks corresponding to three oxidation states of Pt. The most intense doublet peaks at 70.7 eV (Pt $4f_{7/2}$) and 74.7 eV (Pt $4f_{5/2}$) are attributed to the metallic Pt^0. Peaks centered at 73.1 eV (Pt $4f_{7/2}$) and 76.3 eV (Pt $4f_{5/2}$) are assigned to the Pt^{II}, and the broad peak at 77.0 eV is attributed to the Pt^{IV} species.[11] The relative percentages of Pt^0, Pt^{II}, and Pt^{IV} are calculated from the peak areas, which are 62%, 22%, and 16%, respectively. The deconvoluted C 1s spectra of the nanocomposite shows peaks corresponding to C=C, C−C, C−O/O−C−O and C=O/O−C=O centered at 282.2, 283.7, 285.7, and 287.4 eV, respectively.[11] A small peak at 281.1 eV may be assigned to C 1s of the C−X−Pt (X = C/O). A similar XPS study of PdGN shows the presence of Pd^{II} as the major component. In general, it is clearly observed that the double humped peaks of graphene oxide with a higher percentage of oxygenated carbon or sp^3 carbon is drastically reduced upon chemical reduction.[11c,d] The oxidation states of metal in AuGN and AgGN are determined from the optical property and XRD. The presence of a weak plasmon band of gold/silver is observed in AuGN/AgGN, and the signature of metal oxide is observed in XRD, suggesting the presence of a mixture of metal and oxide (Supporting Information, Figures S2 and S11).

Electrocatalytic Performance of Noble Metal−Graphene Nanocomposite. The catalytic performance of MGN is tested for the electrochemical oxidation of formic acid and ethanol[12] (Figures 3 and 4 and Supporting Information, Figures S15−S21). Figure 3 shows the cyclic voltametry curves of formic acid oxidation using PtGN in comparison to three other
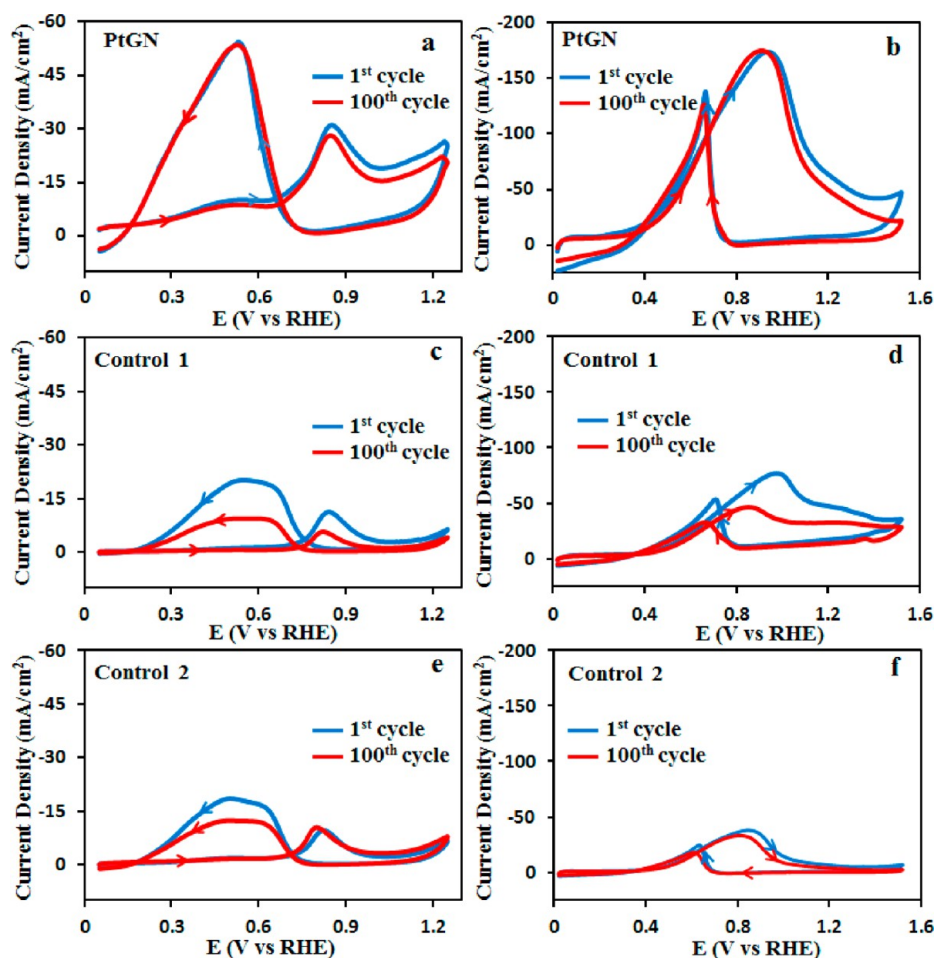
Figure 3. Electrocatalytic oxidation of formic acid (a,c,e) and ethanol (b,d,f) by PtGN in comparison to three different control nanocomposites (current density is based on geometrical surface area). The control 1 nanocomposite is prepared by *in situ* reduction of H_2PtCl_6 by $NaBH_4$ in the presence of partially reduced graphene oxide. Control 2 is a commercially available 20 wt % Pt/C nanocomposite. In each case, a glassy carbon electrode is modified with nanocomposites, and then the oxidation of 0.25 M formic acid and 0.5 M ethanol is performed in 0.5 M H_2SO_4 and 1 M KOH at a scan rate of 50 mV/s.
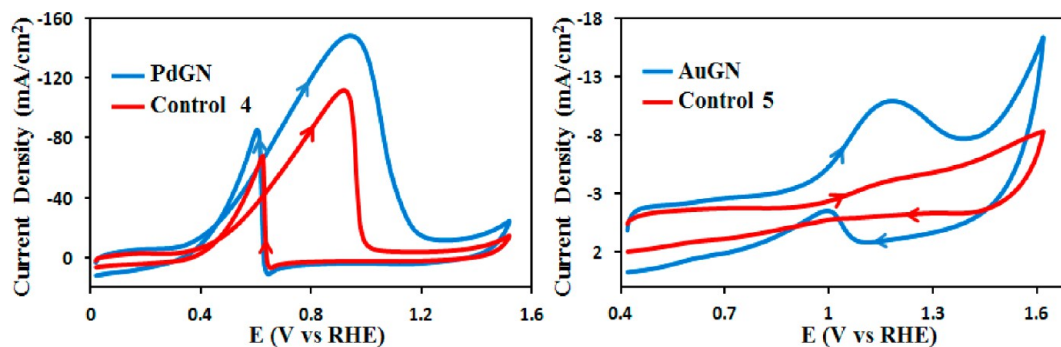

Figure 4. Electrocatalytic oxidation of ethanol by PdGN and AuGN in comparison to control 4 and control 5 (current density is based on geometrical surface area). The control 4 nanocomposite is prepared by *in situ* reduction of $PdCl_2$ by $NaBH_4$ in the presence of partially reduced graphene oxide. Control 5 is synthesized by galvanic reaction between $HAuCl_4$ and partially reduced graphene oxide. A glassy carbon electrode is modified with nanocomposites, and then oxidation of 0.5 M ethanol is performed in 1 M KOH at a scan rate of 50 mV/s.

Pt based nanocomposites. The results show that catalytic formic acid oxidation by PtGN follows two different pathways. The forward scan shows one peak at ~0.5 V which corresponds to direct oxidation of HCOOH to CO_2 and another peak at ~0.85 V which corresponds to the oxidation of adsorbed CO generated in the dehydration step[12c] (i.e., HCOOH converted to CO and H_2O). But the backward scan shows only the intense direct oxidation peak at around 0.53 V without any CO oxidation step. In contrast, other control nanocomposites do not show direct HCOOH oxidation peaks in the forward scan and produce weak and broad peaks in the 0.5−0.72 V region in both forward and backward scans. The peak current intensity at 0.53 V in the backward potential scan is about 3 times higher for PtGN than control nanocomposites, meaning that the

electrochemical activity of PtGN is about 3 times greater than commonly used Pt based nanocomposites. The surface area based specific activities at potential 0.53 V (where current is normalized by active surface area) for PtGN, control 1, and control 2 are −1.34, −0.97, and −0.48 mA cm^{-2}, and mass activities at potential 0.53 V are −0.85, −0.29, and −0.21 A mg^{-1}, respectively. In addition, the catalytic current using PtGN remains unaltered even at the 100th cycle, but for control nanocomposites it is significantly reduced at the 100th cycle (Supporting Information, Figure S20). These results suggest that developed PtGN is more efficient and tolerant of the poisoning effect of CO as compared to control nano-composites.

Similarly, electrocatalytic activity for ethanol oxidation shows higher catalytic current for PtGN than control nanocomposites (Figure 3). The forward and backward currents are observed in between 0.52 and 1.1 V with the corresponding oxidation[12b] of ethanol to CH_3COO^-, and the catalytic current is 2.4−5 times higher than control nanocomposites. The ratio of forward to backward current intensity, which is an index for tolerance of the catalyst[12a,d] toward CO-like carbonaceous poisoning species, is ∼1.32. In addition, no oxidation peak for CO is detected at a higher potential, and no loss of current is observed after 100 cycles, which indicates that the nanocomposites are highly stable without any poisoning intermediates as compared to control nanocomposites. The surface area based specific activity of PtGN (−4.13 mA cm^{-2}) is 1.25 to 4.2 times greater, and the mass specific activity of PtGN (2.8A mg^{-1}) is 2.5 to 8 times greater than control nanocomposites at a potential of 0.93 V. The performance of PdGN and AuGN has also been investigated (Figure 4). The electrochemical ethanol oxidation by PdGN and AuGN shows higher sensitivity compared to control samples. In the case of PdGN, the catalytic current is 1.34 times as intense and the tolerance ratio toward CO is higher (1.8) as compared to the control 4 sample (1.66). Moreover, the current produced up to 100 electrochemical cycles that are reasonably stable (Supporting Information, Figure S20). Similar enhanced electrochemical performance is also observed for formic acid oxidation (Supporting Information, Figure S17).

■ DISCUSSION

There are four tentative reasons for the origin of stable and enhanced electrocatalytic activity. First, the nanoparticles are small and highly dispersed on the graphene backbone, which allows a maximum number of exposed surface metal atoms. Second, MGNs are free from any adsorbed surfactant/stabilizer, and thus all the surface metal atoms are accessible for catalysis. Third, graphene−graphene interaction is at a minimum due to a highly dispersed metal nanoparticle that offers a maximum performance of graphene by enhancing the electron transport from the catalyst site to the electrode. Fourth, mixed valence states of metal provide a metal oxide layer around each metal nanoparticle that helps strong binding with partially reduced graphene oxide and thus offers a stable catalytic current on repeated cycles.

There is a lot of evidence that the redox reaction based chemical linkage between colloidal metal oxide/hydroxide and reduced graphene oxide is the actual driving force for the formation of stable MGN. First, the loading of total metal on MGN depends on the oxidation state of metal and graphene. For example, loading of Pt in PtGN is <1% when colloidal Pt nanoparticles and colloidal graphene oxide are used to make a

nanocomposite, but Pt loading increases from 10% to 20% if colloidal graphene oxide is reduced by hydrazine for shorter and longer time (Supporting Information, Table S3). TEM evidence also supports this result, showing that colloidal Pt^{IV} oxide nanoparticles are heavily attached with partially reduced graphene oxide. However, if colloidal Pt^{IV} oxide is changed to colloidal Pt^0 or partially reduced graphene oxide is replaced by graphene oxide, the attachment of Pt based particles with graphene is significantly lowered (Supporting Information, Figure S6). Second, the mixed oxidation state of metal in the MGN suggests that a part of the metal ion present in colloidal metal oxide is reduced to metal. As no other reducing agents were present, it can be said that the redox reaction between colloidal metal oxide and partially reduced graphene oxide transforms the oxidized metal ion to a metal atom. There is an alternative possibility that hydrazine used during the reduction of graphene oxide might be attached or adsorbed on the graphene surface[9] and be responsible in producing MGN. But a control experiment showed that if H_2PtCl_6 is mixed with partially reduced graphene oxide, no Pt nanoparticle is formed (Supporting Information, Figure S6). The possibility of a proposed redox reaction between graphene oxide and metal oxide is apparent from the oxidation potential of graphene oxide[13] (0.48 V vs SCE) and the reduction potential of PtO$_2$/ PtO and PtO/Pt[14] (in the range of 1.22 to 1.28 V vs SCE), the reduction potential of Au(OH)$_3$/Au (E^0 =1.89 V vs SCE), and the reduction potential of Ag$_2$O/Ag (E^0 = 0.586 V vs SCE). Such a redox reaction is expected to be low for Pd due to the lower reduction potential of Pd(OH)$_2$/Pd[14] (E^0 = 0.314 v vs SCE) that leads to Pd^{II} oxide based PdGN.

The electrochemically active surface area (ECSA) for the PtGN based catalyst is determined from the electric charge of hydrogen adsorption and desorption on Pt surfaces[8c,15] and compared with three control catalysts (Supporting Information, Figure S21). The broad peaks for H adsorption/desorption that are observed here may be due to overlapping of weakly and strongly bonded hydrogen atoms.[13] Results show that the ECSA is ∼65 m^2/g for PtGN, which is around 1.5−4 times higher than three control catalysts (∼30 m^2/g for control 1, ∼45 m^2/g for control 2, and ∼17 m^2/g for control 3). This result clearly shows that PtGN provides an increased active catalytic surface area compared to all the control catalysts. As the Pt loadings are almost the same (17−24 wt %) in all samples and the same amount of material is deposited on the electrode, such an increased catalytic surface area can only be explained by the smaller size of the Pt nanoparticle present in PtGN. The higher ECSAs signify the higher number of catalytically active sites and higher CO tolerance, which are responsible for increased current density during the electro-chemical fuel decomposition. Lower active surface area of control samples indicates the limitation of the conventional chemical reduction based approach that produces Pt nano-particle of >2.5 nm size or the formation of aggregated Pt particles that decreases the active catalytic surface area. The advantage of using colloidal Pt oxide is that it restricts the Pt nanoparticle size <2.5 nm and provides a thin protective oxide layer that stabilizes both the Pt nanoparticle and graphene based composite.

■ CONCLUSION

In summary, we have synthesized a metal nanoparticle and graphene based nanocomposite which is clean, free from surfactant/stabilizer, and acts as a high performance fuel cell

catalyst. The preparation method involves a redox reaction between ultrasmall colloidal metal oxide/hydroxide and partially reduced graphene oxide and the formation of a nanocomposite with small size metal–metal oxide based nanoparticles. The presented Pt and Pd based nanocomposites offer all three advantages that are required for fuel cell catalysts, i.e., it produces a high catalytic current, has a stable current for repeated catalytic cycles, and is easy to prepare. Currently, we are trying to improve the results with a Au/Ag-graphene based nanocomposite via alloying with Pt/Pd.

■ ASSOCIATED CONTENT

Ⓢ Supporting Information

Summary of graphene or graphene oxide based different nanocomposites with reported electrochemical activity, details of different control nanocomposites, results of ICP-AES based determination of metal loading in different nanocomposites, effect of adding different amounts of NaOH solution (1 M) to a 1.5 mL H_2PtCl_6 (10 mM) solution and reaction time in producing colloidal Pt^{IV} oxide, UV–visible absorption spectra, TEM image and size distribution histograms, TEM images of Pt-graphene based nanocomposite prepared under different conditions, low resolution TEM images, XRD spectra, Raman spectra, XPS spectra, effect of NaOH concentration on preparing colloidal Pt^{IV} oxide and its influence on PtGN based fuel cell catalysis, effect of reaction time on preparing colloidal Pt^{IV} oxide and its influence on PtGN based fuel cell catalysis, the electrochemical activity of PdGN and control 4, electrochemical oxidation of formic acid and ethanol by control 3, active surface area based specific activity, stable electrocatalytic current up to 100 electrochemical cycles using PtGN catalyst, and measurement of electrochemically active surface areas. This material is available free of charge via the Internet at http://pubs.acs.org.

■ AUTHOR INFORMATION

Corresponding Author
*Telephone: +91-33-24734971. Fax: +91-33-24732805. E-mail: camnrj@iacs.res.in.

Notes
The authors declare no competing financial interest.

■ ACKNOWLEDGMENTS

■ REFERENCES

(1) Gasteiger, H. A.; Kocha, S. S.; Sompalli, B.; Wagner, F. T. *Appl. Catal., B* **2005**, *56*, 9−35.

(2) (a) Guo, S.; Dong, S.; Wang, E. *ACS Nano* **2010**, *4*, 547−555. (b) Zhang, S.; Shao, Y.; Liao, H.; Liu, J.; Aksay, I. A.; Yin, G.; Lin, Y. *Chem. Mater.* **2011**, *23*, 1079−1081. (c) Huang, X.; Zhao, Z.; Fan, J.; Tan, Y.; Zheng, N. *J. Am. Chem. Soc.* **2011**, *133*, 4718−4721. (d) Ma, L.; Wang, C.; Gong, M.; Liao, L.; Long, R.; Wang, J.; Wu, D.; Zhong, W.; Kim, M. J.; Chen, Y.; Xie, Y.; Xiong, Y. *ACS Nano* **2012**, *6*, 9797−9806.

(3) Murray, C. B.; Kagan, C. R.; Bawendi, M. G. *Annu. Rev. Mater. Sci.* **2000**, *30*, 545−610.

(4) (a) Pileni, M. P. *Nat. Mater.* **2003**, *2*, 145−150. (b) Son, S. U.; Jang, Y.; Yoon, K. Y.; Kang, E.; Hyeon, T. *Nano Lett.* **2004**, *4*, 1147−1151. (c) Wang, L.; Yamauchi, Y. *J. Am. Chem. Soc.* **2009**, *131*, 9152−

9153. (d) Myers, V. S.; Weir, M. G.; Carino, E. V.; Yancey, D. F.; Pande, S.; Crooks, R. M. *Chem. Sci.* **2011**, *2*, 1632−1646.

(5) Li, D.; Wang, C.; Tripkovic, D.; Sun, S.; Markovic, N. M.; Stamenkovic, V. R. *ACS Catal.* **2012**, *2*, 1358−1362.

(6) (a) Xu, C.; Wang, X.; Zhu, J. *J. Phys. Chem. C* **2008**, *112*, 19841−19845. (b) Sharma, S.; Ganguly, A.; Papakonstantinou, P.; Miao, X.; Li, M.; Hutchison, J. L.; Delichatsios, M.; Ukleja, S. *J. Phys. Chem. C* **2010**, *114*, 19459−19466. (c) Ha, H. W.; Kim, I. Y.; Hwang, S. J.; Ruoff, R. S. *Electrochem. Solid-State Lett.* **2011**, *14*, B70−B73. (d) Kundu, P.; Nethravathi, C.; Deshpande, P. A.; Rajamathi, M.; Madras, G.; Ravishankar, N. *Chem. Mater.* **2011**, *23*, 2772−2780. (e) Wang, Y. J.; Wilkinson, D. P.; Zhang, J. *Chem. Rev.* **2011**, *111*, 7625−7651.

(7) (a) Si, Y. C.; Samulski, E. Y. *Chem. Mater.* **2008**, *20*, 6792−6797. (b) Scheuermann, G. M.; Rumi, L.; Steurer, P.; Bannwarth, W.; Mulhaupt, R. *J. Am. Chem. Soc.* **2009**, *131*, 8262−8270. (c) Kamat, P. V. *J. Phys. Chem . Lett.* **2010**, *1*, 520−527. (d) Huang, X.; Yin, Z.; Wu, S.; Qi, X.; He, Q.; Zhang, Q.; Yan, Q.; Boey, F.; Zhang, H. *Small* **2011**, *7*, 1876−1902. (e) Mondal, A.; Sinha, A.; Saha, A.; Jana, N. R. *Chem. Asian J.* **2012**, *7*, 2931−2936. (f) Mondal, P.; Sinha, A.; Salam, N.; Roy, A. S.; Jana, N. R.; Islam, S. M. *RSC Adv.* **2013**, *3*, 5615−5623.

(8) (a) Li, Y.; Gao, W.; Ci, L.; Wang, C.; Ajayan, P. M. *Carbon* **2010**, *48*, 1124−1130. (b) Zhang, S.; Shao, Y.; Liao, H.; Engelhard, M. H.; Yin, G.; Lin, Y. *ACS Nano* **2011**, *5*, 1785−1791. (c) Yang, J.; Tian, C.; Wang, L.; Fu, H. *J. Mater. Chem.* **2011**, *21*, 3384−3390. (d) Qiu, J. D.; Wang, G. C.; Liang, R. P.; Xia, X. H.; Yu, H. W. *J. Phys. Chem. C* **2011**, *115*, 15639−15645. (e) Yin, H.; Tang, H.; Wang, D.; Gao, Y.; Tang, Z. *ACS Nano* **2012**, *6*, 8288−8297. (f) Guo, S.; Sun, S. *J. Am. Chem. Soc.* **2012**, *134*, 2492−2495. (f) Sun, S.; Zhang, G.; Gauquelin, N.; Chen, N.; Zhou, J.; Yang, S.; Chen, W.; Meng, X.; Geng, D.; Banis, M. N.; Li, R.; Ye, S.; Knights, S.; Botton, G. A.; Sham, T. K.; Sun, X. *Sci. Rep.* **2013**, *3*, 1−9. (h) Wang, C.; Ma, L.; Liao, L.; Bai, S.; Long, R.; Zuo, M.; Xiong, Y. *Sci. Rep.* **2013**, *3*, 2580.

(9) Dreyer, D. R.; Park, S.; Bielawski, C. W.; Ruoff, R. S. *Chem. Soc. Rev.* **2010**, *39*, 228−240.

(10) (a) Reetz, M. T.; Koch, M. G. *J. Am. Chem. Soc.* **1999**, *121*, 7933−7934. (b) He, B.; Ha, Y.; Liu, H.; Wang, K.; Liew, K. Y. *J. Colloid Interface Sci.* **2007**, *308*, 105−111. (c) Gao, M. R.; Lin, Z. Y.; Jiang, J.; Cui, C. H.; Zheng, Y. R.; Yu, S. H. *Chem. Eur. J.* **2012**, *18*, 8423−8429. (d) Liu, X.; Li, L.; Meng, C.; Han, Y. *J. Phys. Chem. C* **2012**, *116*, 2710−2719. (e) Liu, X.; Meng, C.; Han, Y. *J. Phys. Chem. C* **2013**, *117*, 1350−1357. (f) Liu, R.; Huang, H.; Li, H.; Liu, Y.; Zhong, J.; Li, Y.; Zhang, S.; Kang, Z. *ACS Catal.* **2014**, *4*, 328−336.

(11) (a) Moulder, J. F.; Stickle, F. W.; Sobol, P. E.; Bomben, K. D. *Handbook of X-ray Photoelectron Spectroscopy*; Perkin-Elmer: Waltham, MA, 1995. (b) Mattevi, C.; Eda, G.; Agnoli, S.; Miller, S.; Mkhoyan, K. A.; Celik, O.; Mastrogiovanni, D.; Granozzi, G.; Garfunkel, E.; Chhowalla, M. *Adv. Funct. Mater.* **2009**, *19*, 2577−2583. (c) Saha, A.; Basiruddin, S. K.; Ray, S. C.; Roy, S. S.; Jana, N. R. *Nanoscale* **2010**, *2*, 2777−2782. (d) Yen, M. Y.; Teng, C. C; Hsiao, M. C.; Liu, P. I.; Chuang, W. P.; Ma, C. C. M.; Hsieh, C. K.; Tsai, M. C.; Tsai, C. H. *J. Mater. Chem.* **2011**, *21*, 12880−12888.

(12) (a) Zheng, S. F.; Hu, J. S.; Zhong, L. S.; Wan, L. J.; Song, W. G. *J. Phys. Chem. C* **2007**, *111*, 11174−11179. (b) Ksar, F.; Surendran, G.; Ramos, L.; Keita, B.; Nadjo, L.; Prouzet, E.; Beaunier, P.; Hagege, A.; Audonnet, F.; Remita, H. *Chem. Mater.* **2009**, *21*, 1612−1617. (c) Zhang, S.; Shao, Y.; Yin, G.; Lin, Y. *Angew. Chem., Int. Ed.* **2010**, *49*, 2211−2214. (d) Shi, J. J.; Yanga, G. H.; Zhu, J. J. *J. Mater. Chem.* **2011**, *21*, 7343−7349.

(13) Chen, X.; Wu, G.; Chen, J.; Chen, X.; Xie, Z.; Wang, X. *J. Am. Chem. Soc.* **2011**, *133*, 3693−3695.

(14) (a) Bard, A. J.; Parsons, R.; Jordan, J. *Standard Potentials in Aqueous Solutions*; IUPAC (Marcel Dekker): New York, 1985. (b) Cotton, F. A.; Wilkinson, G. *Advanced Inorganic Chemistry*, 5th ed.; John Wiley & Sons: New York, 1988.

(15) (a) Sogaard, M.; Odgaard, M.; Skou, E. M. *Solid State Ionics* **2001**, *145*, 31−35. (b) Seger, B.; Kamat, P. V. *J. Phys. Chem. C* **2009**, *113*, 7990−7995.